Evaluation of four calving laws for Antarctic ice shelves

Joel A. Wilner[1], Mathieu Morlighem[1], and Gong Cheng[1]

[1]Department of Earth Sciences, Dartmouth College, Hanover, NH, USA

Correspondence: Joel A. Wilner (joel.a.wilner.gr@dartmouth.edu)

Abstract. Many floating ice shelves in Antarctica buttress the ice streams feeding them, thereby reducing the discharge of icebergs into the ocean. The rate at which ice shelves calve icebergs and how fast they flow determines whether they advance, retreat, or remain stable, exerting a first-order control on ice discharge. To parameterize calving within ice sheet models, several empirical and physical calving "laws" have been proposed in the past few decades. Such laws emphasize dissimilar features, including along- and across-flow strain rates (the eigencalving law), a fracture yield criterion (the von Mises law), longitudinal stretching (the crevasse depth law), and a simple ice thickness threshold (the minimum thickness law), among others. Despite the multitude of established calving laws, these laws remain largely unvalidated for the Antarctic Ice Sheet, rendering it difficult to assess the broad applicability of any given law in Antarctica. We address this shortcoming through a set of numerical experiments that evaluate existing calving laws for ten ice shelves around the Antarctic Ice Sheet. We utilize the Ice-sheet and Sea-level System Model (ISSM) and implement four calving laws under constant external forcing, calibrating the free parameter of each of these calving laws for each ice shelf by assuming that the current position of the ice front is in steady state and finding the set of parameters that best achieves this position over a simulation of 200 years. We find that, in general, the eigencalving and von Mises laws best reproduce observed calving front positions under the steady state position assumption. These results will streamline future modeling efforts of Antarctic ice shelves by better informing the relevant physics of Antarctic-style calving on a shelf-by-shelf basis.

1 Introduction

Iceberg calving is a major component of the mass budget of large ice sheets and marine-terminating glaciers. Currently, calving constitutes approximately 45% of mass loss from Antarctic ice shelves (Rignot et al., 2013) and, together with frontal melt, approximately 40% from the Greenland Ice Sheet (Aschwanden et al., 2019). Accelerated ice discharge through calving amplifies the mass deficit of ice sheets and ice caps, enhancing their contribution to global sea-level rise (Benn et al., 2007b). This contribution is disproportionately large given that calving is highly responsive to initial climate signals, which precipitate rapid glacier retreat (Meier and Post, 1987; Rignot et al., 2003; Benn et al., 2007a). Additionally, by reducing resistive stresses at the glacier base and margins, enhanced calving leads to upstream thinning and acceleration, initiating a strong positive feedback

25   on glacier dynamics that further accelerates ice discharge (e.g., Gagliardini et al., 2010; Choi et al., 2018). Given these dynamic feedbacks, realistic simulation of calving in large-scale ice sheet models is crucial for sea-level rise projections over the course of the 21st century and beyond (e.g., Yu et al., 2017; Amaral et al., 2020).

Despite its central role in projecting sea-level rise, iceberg calving remains a fundamental challenge of ice sheet modeling. Several calving laws have been proposed over the past few decades (e.g., Hughes, 1992; Levermann et al., 2012; Morlighem

30   et al., 2016; Mercenier et al., 2018), but a universal calving law – a reliable predictive mathematical formula for calving – has eluded description and consensus. Proposed calving laws are typically limited by the inherent physical complexity and vast diversity of observed calving processes (Benn et al., 2007b; Bassis and Jacobs, 2013; Benn et al., 2017). These processes range from the consistent detachment of small-scale icebergs from fjord-confined outlet glaciers (typical of Greenland) to the sporadic calving of massive tabular icebergs off of ice shelves (typical of Antarctica) (Vieli et al., 2001; Bassis, 2011). This

35   discrepancy is primarily a function of the predominance of grounded tidewater glaciers in Greenland versus large floating ice shelves in Antarctica. Examples of these respective calving regimes include the well-developed mélange of calving discharge at Jakobshavn Isbræ, Greenland (Amundson et al., 2010; Cassotto et al., 2015) and the large concentrations of tabular icebergs in the Southern Atlantic and Southern Indian Oceans (Tournadre et al., 2012). A satisfactory calving law would be able to describe the processes responsible for Greenland-style and Antarctica-style calving along a mathematical continuum.

40   To parameterize such processes, most numerical models of the Antarctic and Greenland Ice Sheets utilize simple empirical calving laws as boundary criteria, classified into *position* laws and *rate* laws. The former express calving in terms of terminus position change, whereas the latter express calving in terms of iceberg calving rate. Accordingly, position laws parameterize calving at discrete intervals, whereas rate laws parameterize calving continuously. These laws are typically constrained by satellite-derived measurements or inferences of ice velocity, ice stresses, and fjord geometry, among other constraints. Early

45   efforts at calving parameterization expressed calving rate in terms of water depth (e.g., Brown et al., 1983) or forced terminus thickness to exceed a value controlled by some calving criterion (e.g., Van Der Veen, 1996; Pfeffer et al., 1997). However, these laws had difficulty applying to both glaciers with grounded and floating termini (Amundson and Truffer, 2010). The crevasse depth law of Benn et al. (2007b) was one of the first to overcome this difficulty, predicting calving to occur when the depth of surface crevasses equals the freeboard (i.e., ice surface height above water level). In this scenario, calving is

50   effectively governed by longitudinal strain rate, which exerts a first-order control on crevasse depth. Despite the success of a strain-based law at bridging the gap between grounded and floating termini, inconsistencies persisted when describing a range of calving behaviors, prompting the development of new calving laws (Amundson and Truffer, 2010). Examples of such laws include an extension of the crevasse depth law that incorporates propagation of basal crevasses (Nick et al., 2010); an application of the crevasse depth law to floating ice shelves (CD; Pollard et al., 2015); the eigencalving law (EC; Levermann

55   et al., 2012), an expression of calving rate as proportional to the product of strain rates parallel and perpendicular to flow; the von Mises law (VM; Morlighem et al., 2016), reliant on tensile stresses and frontal velocities; and a simple minimum thickness threshold (MT). In contrast to these semi-empirical laws, a class of laws has emerged that describe calving through predominantly physical means. Such laws incorporate a continuum damage framework (e.g., Duddu et al., 2013), linear elastic fracture mechanics (Yu et al., 2017), or a combination of the two (Krug et al., 2014).

The development of increasingly complex calving laws has outpaced law validation, leading to significant uncertainty in the applicability of calving laws at the ice-sheet scale (Benn et al., 2017; Amaral et al., 2020). Where data are readily available, calving laws tend to be tuned to specific glaciers or regions, failing to generalize for a range of calving behaviors (Benn et al., 2007b; Bassis, 2011). To overcome this problem, two studies have systematically compared calving laws between different outlet glaciers in Greenland (Choi et al., 2018; Amaral et al., 2020). Choi et al. (2018) simulated glacier flow from 2007 to 2017 with five different calving laws: height above buoyancy (Vieli et al., 2001), the crevasse depth laws of Benn et al. (2007b) and Nick et al. (2010), EC, and VM. In general, VM was found to most closely reproduce observed terminus position change of the nine Greenland outlet glaciers under consideration, with EC performing the poorest. Notably, the authors cautioned that the discharge of large tabular icebergs in Antarctica is likely governed by different physical principles so the results cannot be considered universal. Amaral et al. (2020) evaluated three position laws (the crevasse depth law of Nick et al. (2010), height above flotation, and fraction above flotation) and three rate laws (the stress maximum law of Mercenier et al. (2018), EC, and VM), comparing flowline dynamics against spatially and temporally diverse observations of 50 tidewater glaciers in Greenland. Unlike Choi et al. (2018), Amaral et al. (2020) concluded that the crevasse depth law of Nick et al. (2010) captures observed terminus dynamics with high fidelity. Moreover, Amaral et al. (2020) found that rate-based laws tend to produce high misfit values, particularly for large ablation rates, and struggle to reproduce seasonal and short-term variability. The disparate results of Choi et al. (2018) and Amaral et al. (2020) may be attributed to their contrasting modeling strategies, as the former study utilized the Ice-sheet and Sea-level System Model (ISSM; Larour et al., 2012) with the 2-D Shelfy-Stream Approximation (SSA; Morland and Zainuddin, 1987; MacAyeal, 1989) and a level-set method (Bondzio et al., 2016) to track calving front positional changes whereas the latter study employed a simpler 1-D flowline approach. Another important distinction is that Choi et al. (2018) calibrated calving law tuning parameters on a glacier-specific basis, whereas Amaral et al. (2020) made use of a uniform tuning parameter value across a more extensive suite of glaciers.

To date, calving laws have not been systematically compared for Antarctic ice shelves, rendering it difficult to assess the broad applicability of any given calving law in simulations of Antarctic Ice Sheet dynamics. Here, we follow the approach of Choi et al. (2018) in comparing calving laws for Antarctica, reasoning that the SSA is well suited to model Antarctic ice shelves and that calibrating tuning parameters specific to each ice shelf is a necessary step to optimize calving law performance. However, unlike in Greenland, where calving events are frequent and there are abundant temporal changes in front positions to compare models against, calving events in Antarctica are typically episodic, in some instances only occurring once per several decades for a given portion of the ice margin (Fricker et al., 2002). For this reason, we conclude that it would be impractical to compare modeled front positions for Antarctica against a series of observed changes in front position. Thus, a key difference between our methodology and that of Choi et al. (2018) is that we instead assume that the modern front position is in steady state and try to attain the modeled front that most closely replicates this one position over a 200-year run under constant forcing.

We ascertain that calving processes at different ice shelves may be governed by dissimilar physical principles as a consequence of varying degrees of lateral confinement (among many other potential factors), and that unique tuning parameter values must be determined accordingly. To this end, we implement four different calving laws in ISSM: EC, VM, MT, and CD. We apply these calving laws to ten Antarctic ice shelves, selected on the basis of their size or abundance of observational

95   data. Each calving law has one or two free tuning parameters, calibrated by running 200-year forward models of each ice shelf and determining which parameter value most closely fits the modern-day observed calving front position under a steady state assumption. We then compare the four calibrated calving laws to each other for each ice shelf, determining which calving law best captures a steady state front position on a shelf-by-shelf basis. We quantify possible correlates to calving law success, including frontal velocity, thickness, and buttressing force. Finally, we discuss the implications of these results for ice sheet

100   projections in a warming climate.

2   Methods

Like Choi et al. (2018), we use ISSM to implement four calving laws (EC, VM, MT, and CD) for ten ice shelves: Amery, Denman, Filchner, Larsen C, Pine Island, Ronne, Ross, Shackleton, Thwaites, and Totten Ice Shelves. Mesh resolution increases with proximity to the observed calving front, with a highest resolution of 1 km near the calving front, and is isotropically

105   adapted according to ice velocity. Larger ice shelves such as Ross and Ronne are prescribed a coarser maximum resolution (3 km) for computational efficiency. Typical mesh size for all ice shelves is on the order of tens of thousands of elements. We find that increasing the mesh resolution further does not influence our main results in any significant way. The calving front position is defined using the level-set method (Bondzio et al., 2016). Surface elevation and bed topography data are taken from BedMachine Antarctica V3 (Morlighem et al., 2020). Observed ice velocity data are retrieved from the NASA Making

110   Earth System Data Records for Use in Research Environments (MEaSUREs) dataset, which uses satellite-derived, phase-based InSAR and tracking measurements to derive ice velocity over the period of 2007 to 2018 (Mouginot et al., 2019). As in Choi et al. (2018), surface mass balance (SMB) input is kept constant over the simulation period and is derived from the Regional Atmospheric Climate Model (RACMO2.3), averaged over 1979–2011 (Noël et al., 2015). Our ice shelf models are initialized by first inverting for ~~rigidity~~ the ice viscosity parameter B over floating regions of the domain followed by inverting for basal

115   friction in grounded regions. The final model domain comprises primarily floating ice and, in most cases, a small portion of the adjacent grounded ice. Upstream boundary conditions at the grounding line utilize observed velocities with fixed ice thickness. Sub-shelf melting is constrained by the dataset of Rignot et al. (2013). To reiterate, we seek the modeled calving front that most closely matches the shape and position of the modern observed front, assumed to be in steady state because calving in Antarctica occurs so infrequently, unlike in Greenland. We set the transient model to run for an arbitrarily long time of 200

120   years, which we deem long enough to attain a modeled steady state calving front position for calibrated tuning parameters. For reference, we quantify drift in ice volume, mean ice thickness, and mean ice velocity over this simulation period for each ice shelf with a fixed ice front (Figs. S1-S10). We note that the more dynamic ice shelves exhibit greater drift, likely due to inconsistencies between the applied sub-shelf melt rates and our steady state assumption.

2.1 Calving laws

125   Three of the four calving laws used here are rate-based laws (EC, VM, and CD), whereas MT is a position-based law. EC defines calving rate c as proportional to along- and across-flow strain rate, such that

$$c = K\,\dot{\epsilon}_{\parallel}\,\dot{\epsilon}_{\perp}, \tag{1}$$

where K is a proportionality constant that encapsulates the material properties of ice relevant to calving, $\dot{\epsilon}_{\parallel}$ is along-flow strain rate, and $\dot{\epsilon}_{\perp}$ is across-flow strain rate (Levermann et al., 2012). By definition, the EC law contains a first-order dependence on

130   the spreading rate tensor and thus may be suited to capture calving behavior of ice shelves in unconfined embayments. We take K to be the tuning parameter for EC in our calibration experiments.

    Within VM, c is proportional to the tensile stress regime at the ice front. Mathematically, this is represented as

$$c = |\boldsymbol{v}|\,\frac{\tilde{\sigma}}{\sigma_{\max}}, \tag{2}$$

where $\boldsymbol{v}$ is the ice front velocity vector, $\tilde{\sigma}$ is the total tensile von Mises stress at the ice front, and $\sigma_{\max}$ is the tensile stress

135   threshold (taken to be the tuning parameter for VM). Without considering any additional undercutting at the ice front, retreat occurs when $\tilde{\sigma}$ exceeds $\sigma_{\max}$, and advance occurs when $\tilde{\sigma}$ is less than $\sigma_{\max}$. Total von Mises tensile stress $\tilde{\sigma}$ is defined as

$$\tilde{\sigma} = \sqrt{3}B\tilde{\dot{\varepsilon}}_e^{1/n}, \tag{3}$$

where B is the ice viscosity parameter, n is Glen's law exponent (taken here to be 3), and $\tilde{\dot{\varepsilon}}_e$ is the effective tensile strain rate, itself proportional to the eigenvalues of the 2-D horizontal strain rate tensor $\dot{\varepsilon}_1$ and $\dot{\varepsilon}_2$ (Morlighem et al., 2016):

140   $$\tilde{\dot{\varepsilon}}_e = \frac{1}{2}\left(\max(0,\dot{\varepsilon}_1)^2 + \max(0,\dot{\varepsilon}_2)^2\right). \tag{4}$$

    The third and final rate law considered here, CD, is a modification of the ice shelf calving criterion introduced by Pollard et al. (2015). Although the crevasse depth laws of Benn et al. (2007b) and Nick et al. (2010) do allow for the development of floating ice tongues, those parameterizations are not initially tuned for large floating ice shelves. In addition, a satisfactory crevasse depth law for floating ice shelves would ideally account for such factors as the discrepancy in ice velocity at the grounding

145   line versus shelf interior and edge points, as in Pollard et al. (2015). Their initial parameterization of incipient dry-surface and basal crevasse depths d_s and d_b, respectively, follows Nick et al. (2010). Dry-surface crevasse depth is parameterized as

$$d_s = \frac{2}{\rho_i g}\left(\frac{\nabla \cdot \boldsymbol{v}}{A}\right)^{\frac{1}{n}}, \tag{5}$$

where $\nabla \cdot \boldsymbol{v}$ is ice divergence, A is the depth-averaged ice rheological coefficient, g is gravitational acceleration, and ρ_i is ice density. Basal crevasse depth is parameterized as

150   $$d_b = \left(\frac{\rho_i}{\rho_w - \rho_i}\right)\frac{2}{\rho_i g}\left(\frac{\nabla \cdot \boldsymbol{v}}{A}\right)^{\frac{1}{n}}, \tag{6}$$

where ρ_w is the density of ocean water. Pollard et al. (2015) include a velocity dependency, parameterizing additional crevasse deepening d_a of incipient fractures as

$$d_a = h \ \max[0, \ln(|\boldsymbol{v}|/1600)]/\ln(1.2) \tag{7}$$

where h is the local ice thickness and $\boldsymbol{v}$ is here expressed in units of m yr^{-1}. The constants in this equation are values calibrated by Pollard et al. (2015) to match velocity observations of Ross and Ronne Ice Shelves as case examples. That is, d_a is tuned to approach h as local ice speed increases to $\sim$1900 m yr^{-1}, speeds observed in the fast-flowing outer regions of Ross and Ronne Ice Shelves. For speeds up to 1600 m yr^{-1}, d_a is zero. A crevasse depth component d_t which accounts for thin floating ice is introduced:

$$d_t = h \ \max[0, \min[1, (150 - h)/50]]. \tag{8}$$

This equation has the practical effect of removing unrealistically thin floating ice less than 100 to 150 m thick. Although this prevents small tidewater glaciers from extending into ice shelves, such small glaciers are excluded from our study. A final crevasse depth component d_w is imposed by Pollard et al. (2015), accounting for the additional opening stress of liquid water in surface crevasses:

$$d_w = 100 \ R^2 \tag{9}$$

where R is annual surface melt plus liquid rainfall remaining after refreezing (in m yr^{-1}). We account for this term through the constant SMB derived from RACMO2.3. Taken together, these individual crevasse depth components can be expressed as a ratio to ice thickness:

$$r = \frac{d_s + d_b + d_a + d_t + d_w}{h}, \tag{10}$$

and finally an overall calving rate (here in m yr^{-1}) is obtained:

$$c = \dot{M}_{\max} \ \max\left(0, \min\left(1, \frac{r - r_c}{1 - r_c}\right)\right), \tag{11}$$

where $\dot{M}_{\max}$ is the maximum migration rate of the ice front (in m yr^{-1}) and r_c is some critical value for calving onset between 0 and 1. We take $\dot{M}_{\max}$ and r_c as the tuning parameters for the CD law. Note that we cap $\dot{M}_{\max}$ at 10 km yr^{-1} for all calving laws to prohibit unrealistically large advance or retreat, but since $\dot{M}_{\max}$ is a tuning parameter for CD, we vary it between 2 km yr^{-1} and 10 km yr^{-1} during CD calibration.

The MT law, which differs from the other three laws considered here in that it is a position law, simply states that calving occurs when $h \leq h_{\min}$, where $h_{\min}$ is some minimum ice thickness threshold, taken here as a tuning parameter.

2.2 Calibration procedure

To calibrate the four calving laws, we perform a series of tests to compute a misfit metric for each ice shelf. First, we calculate the area of the region between the observed modern-day ice shelf front and the modeled front after the simulation period of

180   200 years. We then divide this area by the length of the observed modern-day front to obtain a misfit (in km). Note that this definition does not consider the sign of the misfit; the misfit is agnostic to retreat or advance. A key assumption of this misfit calculation is that the ice shelf front is in a steady state position. This assumption generally holds true for the ice shelves under consideration, which calve sporadically enough that their front positions over the past few decades have been roughly constant. A major exception to this assumption is Thwaites Ice Shelf, whose front is much more dynamic than that of other ice shelves

185   under consideration, but we have included it in this study for the sake of completeness and its importance to the stability of the West Antarctic Ice Sheet.

     We compute the misfit metric for a range of values of each calving law's tuning parameter(s), taking the best-fit as the value that minimizes the misfit (Fig. 1). In constraining the precision of the calibration, we vary the tuning parameter at intervals of 5 kPa for σ_{max} of VM, 5 m for h_{min} of MT, and 0.1 and 2 km for r_c and $\dot{M}_{\mathrm{max}}$, respectively, of CD. The calibration precision

190   for K of EC varies by ice shelf: 0.5×10^7 m$\times$yr for Filchner, Amery, and Denman, and 0.5×10^8 m$\times$yr for all other ice shelves except Larsen C (0.5×10^{10} m$\times$yr). The typical outcome of the calibration process is a curve with one branch representing retreat from the modern-day observed front and another branch representing advance, as shown in Figs. 1d-g for Ross Ice Shelf. Fig. 1a and Fig. 1c show the most extreme retreat and advance scenarios, respectively, modeled for EC. The optimal steady state (Fig. 1b) occurs for a tuning parameter value where the misfit metric is minimized on the calibration curve.

195 **3   Results**

    Tuning parameter calibration results are shown in Table 1. Notably, the chosen K values of EC range 4 orders of magnitude, with Larsen C being an upper outlier. The chosen σ_{max} values of VM are generally consistent with each other (same order of magnitude), while the chosen h_{min} values of MT are largely dependent on the original thickness of the ice shelf. The chosen CD parameter value r_c ranges greatly between 0 and 1, signifying a diversity of critical crevasse depth thresholds, while the

200   corresponding CD parameter $\dot{M}_{\mathrm{max}}$ is typically minimized at 2 km except for the three largest ice shelves, Ross, Ronne and Filchner.

    The calibration results visualized for Ross Ice Shelf represent an ideal scenario where one calving law (EC) performs markedly better than the others at minimizing misfit between initial and modeled fronts (Fig. 1d-g). In this example, EC closely attains the shape and position of the assumed steady state observed calving front (Fig. 1b). As such, in ascertaining

205   calving law success, it is instructive to consider not only the quantitative misfit metric but to also qualitatively assess how well the modeled front captures the shape and position of the observed front.

    We now present results for all ice shelves under consideration, roughly grouped by region. Only one calving law, VM, captures the modern-day calving front position of Larsen C Ice Shelf with any fidelity (Fig. 2a). Interestingly, EC results in considerable ice advance in the region immediately adjacent to Gipps Ice Rise and downstream of the Kenyon Peninsula. The

210   spatial distribution of this advance stands in contrast to the notion that ice flow becomes less constrained by the lateral shear margins after passing Kenyon Peninsula (Wang et al., 2022), since regions of decreased lateral confinement, and thus enhanced lateral strain rate, are expected to increase calving rates under the EC framework (Eq. 1). Both MT and CD result in considerable
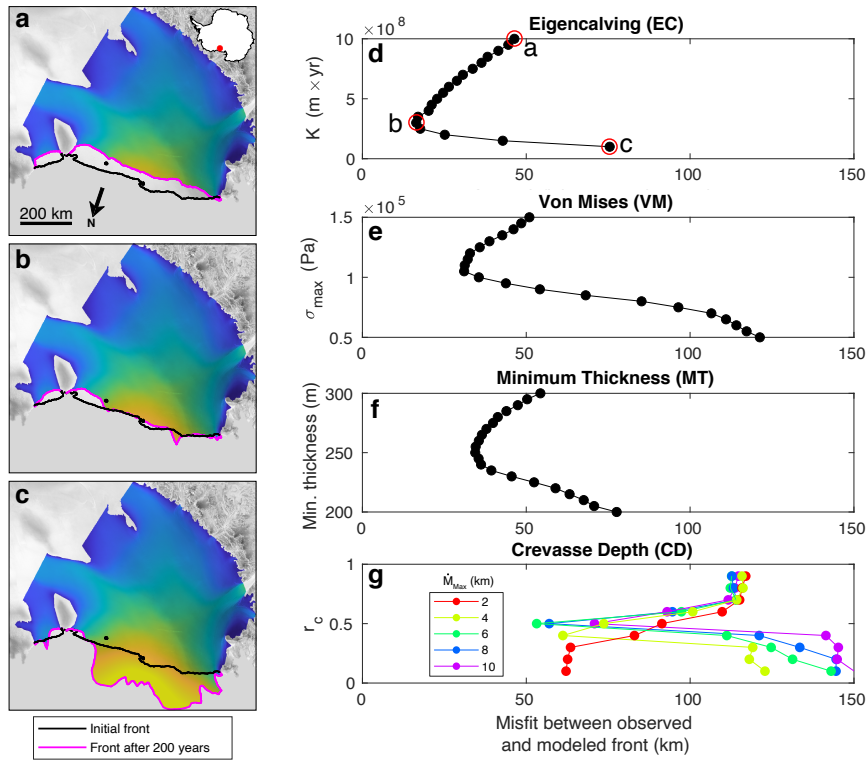
Figure 1. Example of the calibration process for Ross Ice Shelf. Representative results showing **(a)** retreat, **(b)** steady state, and **(c)** advance for eigencalving are shown on the left along with modeled ice velocity in $\log_{10}$ scale from 1 m/yr (blue) to 1000 m/yr (yellow). Calibration curves for the tuning parameters of **(d)** EC, **(e)** VM, **(f)** MT, and **(g)** CD are shown on the right for misfit distances between 0 and 150 km. EC tuning parameter values corresponding to model scenarios **(a)**, **(b)**, and **(c)** are circled in panel **(d)**. Model results are overlaid with a radar image from the RADARSAT-1 Antarctic Mapping Project (RAMP) Antarctic Mapping Mission (AMM-1) (Jezek, 1999) in grey, and the location of Ross Ice Shelf is shown by a red dot on an Antarctica inset.

retreat in the southern portion of the ice shelf, with MT exhibiting pronounced advance in the central portion. Notably, the divide between advance and retreat produced by MT closely follows the arcuate downstream profile of ice extending from Kenyon

215 Peninsula. Qualitatively, misfit is consistently minimized by VM across the extent of the ice shelf front, and the associated misfit value of 6.0 km is more than twice as favorable as the next best misfit value (EC; 12.7 km). CD (22.1 km) and MT (35.8 km) have markedly larger misfit values for Larsen C. Ronne Ice Shelf is best fit by EC (5.7 km), followed by VM (18.2 km), MT (23.8 km), and CD (29.0 km). EC and VM capture the shape and position of the front well except for a south-central region where EC results in a thin protruding ice tongue, coincident with a broader ice tongue associated with VM (Fig. 2b). MT and

220 CD exhibit undulating front shapes which do not closely replicate Ronne's sublinear front. In contrast to Ronne, Filchner Ice Shelf is best fit by VM (4.9 km), followed by CD (9.2 km), MT (21.1 km), and EC (28.9 km). Only VM adequately captures

Ice Shelf	Calving calibration parameter				
	K of EC $\times 10^8$ (m×yr)	σ_{max} of VM (kPa)	h_{min} of MT (m)	r_c of CD (unitless)	$\dot{M}_{\text{max}}$ of CD (km)
Amery	0.50	150	235	0.4	2.0
Denman	0.20	400	215	0.9	2.0
Filchner	1.5	200	440	0.5	8.0
Larsen C	300	140	230	0.5	2.0
Pine Island	3.0	275	390	0.9	2.0
Ronne	4.0	120	280	0.5	6.0
Ross	3.0	105	250	0.5	6.0
Shackleton	2.0	280	55	0.9	2.0
Thwaites	2.0	320	395	0.1	2.0
Totten	2.5	260	410	0.5	2.0

Table 1. Tuned calibration parameter values that minimize the misfit metric, by ice shelf. CD parameter values (r_c and $\dot{M}_{\text{max}}$) are to be taken in combination.
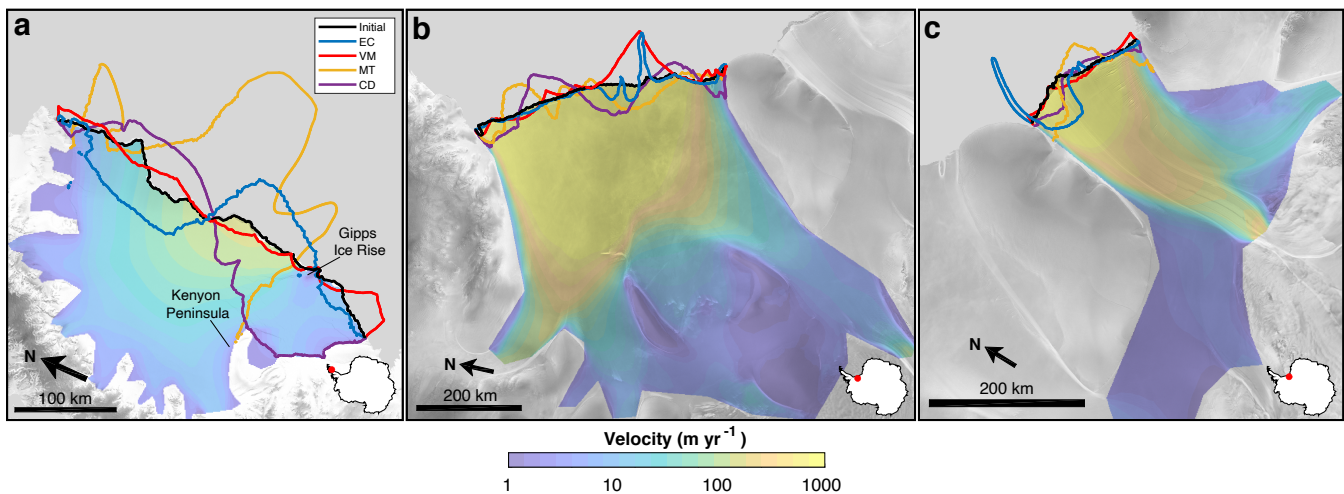
Figure 2. Model results for **(a)** Larsen C, **(b)** Ronne and **(c)** Filchner Ice Shelves. The modeled front positions for each calving law are shown in different colors, along with the initial observed front in black. Ice shelf location is shown by a red dot on an Antarctica inset. Model results and observed velocities are overlaid with a radar image from RAMP AMM-1 (Jezek, 1999) in grey.

the western portion of the shelf; the other calving laws struggle to replicate the frontal shape and position, generating too much retreat and, in the case of EC, producing an extensive ice tongue at the western shelf margin (Fig. 2c).

Pine Island and Ross Ice Shelves are best fit by EC (both 16.4 km) and Thwaites is best fit by CD (5.7 km). For Pine Island, the next best calving laws are VM (20.1 km), MT (20.4 km), and CD (47.1 km); for Thwaites, the next best calving laws are EC (6.4 km), VM (7.4 km), and MT (7.8 km); and for Ross, the next best calving laws are VM (31.0 km), MT (34.4 km), and CD (53.2 km). All four calving laws, particularly CD, result in some level of frontal irregularity for Pine Island, though VM
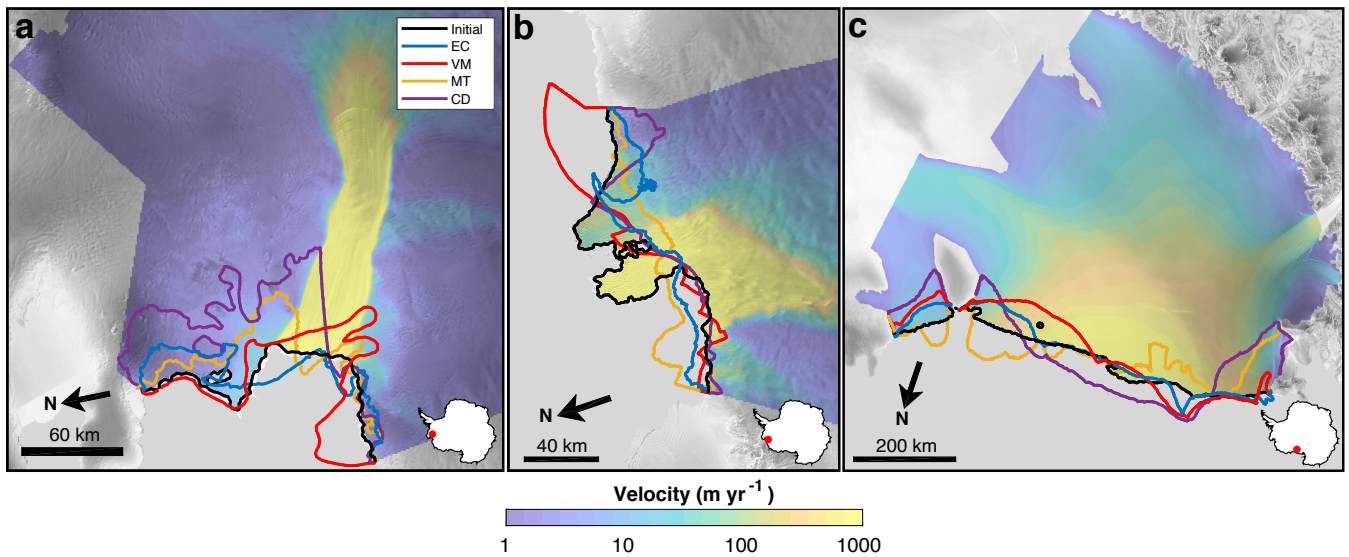
Figure 3. Model results for **(a)** Pine Island, **(b)** Thwaites and **(c)** Ross Ice Shelves. The modeled front positions for each calving law are shown in different colors, along with the initial observed front in black. Ice shelf location is shown by a red dot on an Antarctica inset. Model results and observed velocities are overlaid with a radar image from RAMP AMM-1 (Jezek, 1999) in grey.

captures the northern portion of the front with high fidelity (Fig. 3a). None of the four calving laws replicate the observed ice tongues in the central portion of Thwaites, but CD and VM replicate the front position of the western portion of Thwaites with some success (Fig. 3b). With the exception of a small ice tongue produced in the western portion of the front and some retreat in the eastern portion, EC generally maintains the frontal shape and position of Ross Ice Shelf, in keeping with minimizing the misfit metric (Fig. 3c).

For Amery Ice Shelf, we observe that the best-fit model runs of EC and VM produce ice fronts inverse in shape to each other, with concave and convex fronts, respectively (Fig. 4a). The convex front of VM more closely aligns with the modern-day observed front that extends beyond the embayment under our assumption of steady state front position. Indeed, out of the four calving laws for Amery, VM minimizes the misfit metric (9.2 km), followed by MT (9.5 km), EC (17.3 km), and CD (21.2 km). MT performs reasonably well at capturing the shape and position of the front, particularly in the easternmost portion, though it overestimates advance for the westernmost half. The misfit values of VM and MT are nearly the same, whereas EC and CD perform markedly worse both in both quantitative and qualitative senses, with large regions of retreat with respect to the modern-day observed front. Shackleton Ice Shelf involves a moderate level of modeled frontal irregularity, though VM (3.5 km) and EC (3.7 km) capture the observed central protrusion of the ice front reasonably well (Fig. 4b). MT (6.1 km) and CD (8.2 km) truncate this protrusion. Modeled fronts for Denman Ice Shelf are irregularly shaped, with the best-fit law VM (3.5 km) replicating the easternmost portion of the front well but overestimating advance in the westernmost portion (Fig. 4c). EC (7.5 km) and MT (9.6 km) exhibit highly irregular patterns of retreat, and CD (13.1 km) produces a long and spurious ice tongue. All calving laws perform reasonably well for Totten Ice Shelf, with low misfit values of <5 km, though only EC (1.9
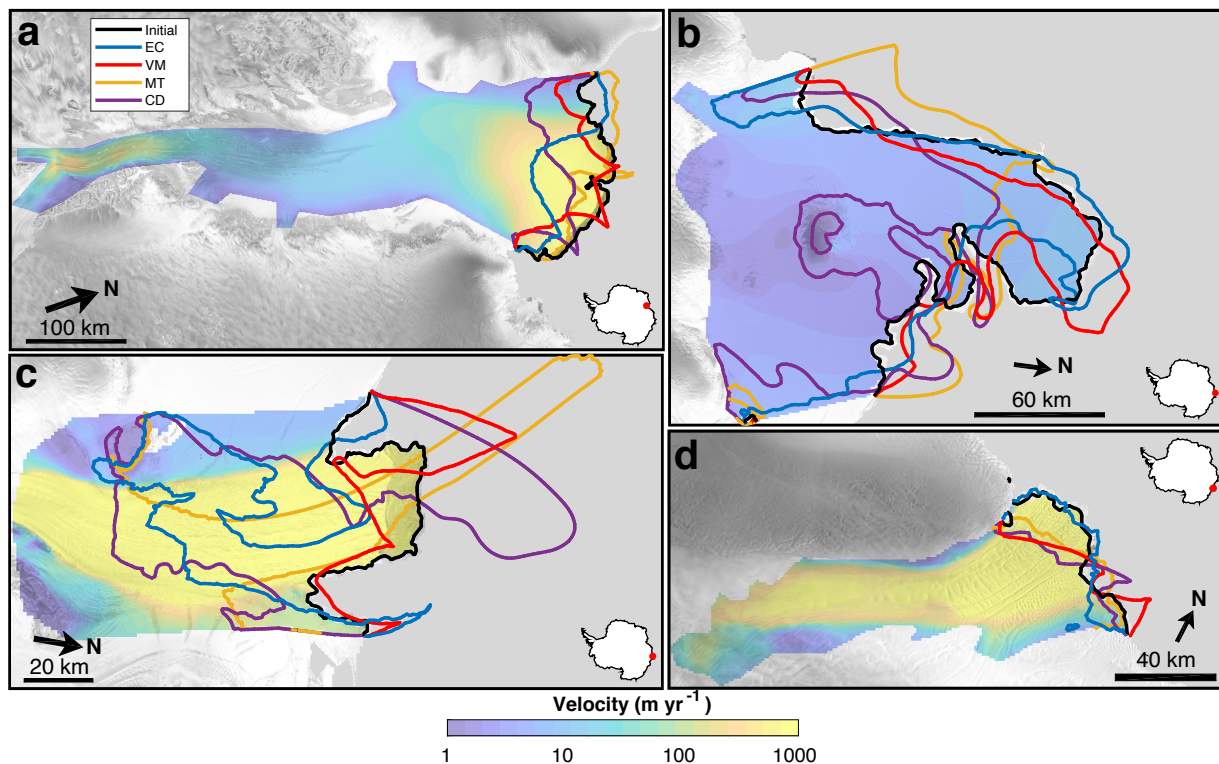
Figure 4. Model results for **(a)** Amery, **(b)** Shackleton, **(c)** Denman, and **(d)** Totten Ice Shelves. The modeled front positions for each calving law are shown in different colors, along with the initial observed front in black. Ice shelf location is shown by a red dot on an Antarctica inset. Model results and observed velocities are overlaid with a radar image from the RAMP AMM-1 (Jezek, 1999) in grey.

km) accurately captures the convexity of the ice front (Fig. 4d). MT (4.0 km), VM (4.1 km) and CD (4.5 km) all exhibit retreat in the convex portion of the ice shelf. EC does produce some retreat in the eastern region where MT and CD replicate the observed front, but we deem this region to be insignificant compared to the bulk of the calving front which does demonstrate affinity to EC.

250   The overall results indicate that 9 of the 10 ice shelves under consideration are best captured by either EC (Pine Island, Ronne, Ross, and Totten) or VM (Amery, Denman, Filchner, Larsen C, and Shackleton), assuming our steady state assumption of front position (Fig. 5). In some cases, such as VM versus MT for Amery and VM versus EC for Shackleton, the best-fit calving law is only marginally better than the second-best. MT results in several unacceptably large misfits (Filchner, Larsen C, Ronne, and Ross), as does CD (Pine Island, Ronne, and Ross). EC misfit is unacceptably large for Filchner, but maintains a

255 low value for most other ice shelves, relative to the original size of the ice shelf. Only Thwaites Ice Shelf is best characterized by a calving law other than EC or VM (CD), though it is important to reiterate that Thwaites exhibits more dynamic behavior than the other ice shelves considered here.

4 Discussion

Given the results of Fig. 5, it is instructive to consider why EC and VM perform best for the majority of ice shelves under
260 consideration. A first-order answer may invoke the notion that EC is, in some sense, tuned to follow embayment coastlines,
and VM is tuned to ice velocity profiles. This occurs on account of their formulations, with EC increasing calving rate when ice
exits an embayment (by virtue of across-flow strain rate increasing; see Eq. 1) and VM increasing calving rate where velocity
increases (see Eq. 2). As a consequence, ice shelves whose fronts already follow coastlines may tend to favor EC, while ice
shelves with more complex velocity profiles may be "evened out" by VM. By contrast, MT and CD are highly dependent on
265 local conditions, particularly ice thickness, that may vary on small spatial scales. This may render MT and CD unlikely to
consistently capture front-wide calving processes that operate on larger spatial scales.

Taking EC and VM to be the most effective calving laws of the four considered, we next investigate the possible correlates
that predict EC success versus VM success for any given ice shelf. Performing two-sample t-tests (with the important caveats
that data are not normally distributed and sample size is exceedingly small, with $n = 9$), we find no significant differences
270 in mean frontal thickness or mean frontal velocity between those ice shelves best characterized by EC versus VM. Another
potential factor that does not yield a significant difference is mean water depth along the front. With these factors unlikely to
be predictive correlates, we turn to the role of buttressing as a possible predictor of calving law success. Buttressing is a natural
avenue to explore, as previous work has implied a relationship between ice shelf weakening, reduced buttressing, and calving
(Borstad et al., 2016). We reproduce the buttressing calculations of Fürst et al. (2016) to quantify buttressing along the second
275 principal stress direction ("maximum buttressing", in keeping with the existing nomenclature) and along the flow direction
("flow buttressing") over the entire floating extent of the ice shelf. As in Fürst et al. (2016), we compute a normal buttressing
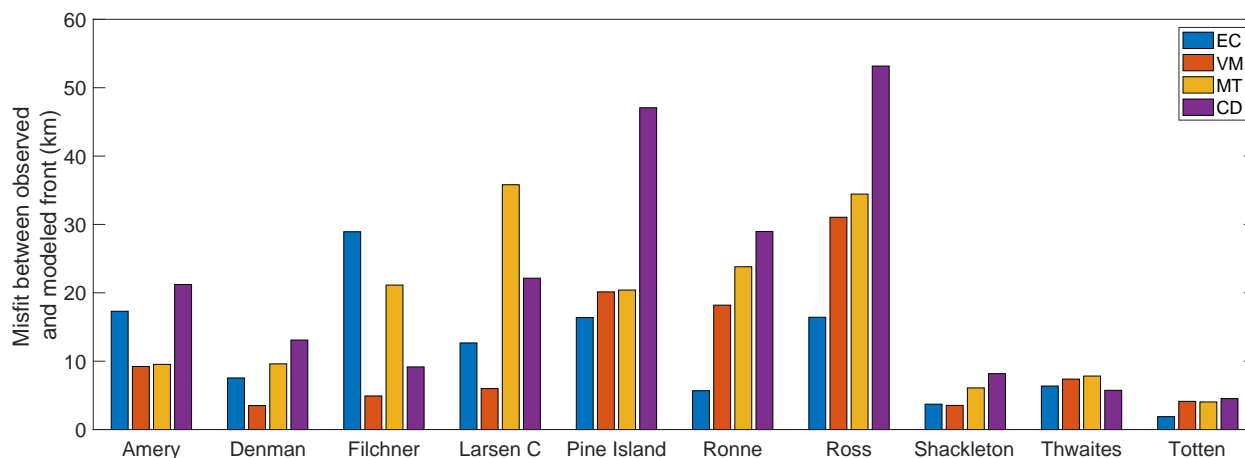
Figure 5. Modeled misfit distances for each calving law by ice shelf.

number K_n, such that

$$K_n = 1 - \frac{\boldsymbol{n} \cdot \sigma \cdot \boldsymbol{n}}{N_0}, \tag{12}$$

where $\boldsymbol{n}$ is a unit vector either in the direction of the second principal stress (for maximum buttressing) or the flow direction (for flow buttressing), σ is the resistive stress tensor, and N_0 is the vertically integrated pressure exerted by the ocean on the ice front:

$$N_0 = \frac{1}{2}\rho_i \left(1 - \frac{\rho_i}{\rho_w}\right) gh. \tag{13}$$

Computing mean values of maximum buttressing and flow buttressing along ice shelf fronts, we again find no significant differences between ice shelves best characterized by EC versus those best characterized by VM. Also computing the mean value of maximum buttressing along the grounding line yields no significant difference.

To take a different approach, we next compute the mean buttressing value over the entire ice shelf rather than along the front or grounding line. We use this value to calculate the proportion of "passive shelf ice" (PSI), defined by Fürst et al. (2016) as those regions of shelf ice which have little or no dynamical influence; in other words, PSI does not significantly alter the flow or stress regime if removed. We set different thresholds for computing PSI area based on maximum buttressing values, ranging from 0.1 to 1 at intervals of 0.1. From here, we calculate the percentage of the entire shelf containing PSI according to each buttressing threshold, and compare EC- and VM-best ice shelves. We find that, across all PSI thresholds, ice shelves fit best by VM nominally have a greater proportion of PSI than those fit best by EC (Fig. 6). Initial PSI fraction shown for each ice shelf individually substantiates this notion (Fig. S11). This apparent pattern implies that EC is better tuned to buttressed embayments, and VM is more robust to unbuttressed ice extending outside of embayment margins. Note that buttressing can exceed 1 when opposing ocean pressure and lateral confining pressure exceed the ice flow driving force, in which case ice is in a highly compressive regime. Similarly, the buttressing value can be less than zero when ice is in a purely extensive stress regime (Fürst et al., 2016). It is important to caution that the method of Fürst et al. (2016) is only one of several ways to calculate buttressing and has been challenged in its suitability to measure grounding line buttressing (Zhang et al., 2020). Moreover, the buttressing value strongly depends on the direction chosen at any given point.

To illustrate how EC and VM may exploit the same buttressing regime in different ways, consider Fig. 7. Here, we show the evolution of buttressing for floating ice over the 200-year model simulation. For Amery Ice Shelf, VM maintains the original unbuttressed extent outside of the embayment (Figs. 7a and 7g), while EC removes the unbuttressed extent outside of the embayment and trends roughly towards the embayment cutoff (Figs. 7a and 7d). For Ross and Ronne Ice Shelves, VM allows unbuttressed ice to advance beyond the embayment coastline (Figs. 7h and 7i, respectively). By contrast, EC maintains ice at approximately the extent of the embayment coastline (Figs. 7e and 7f), with some thin ice tongues advancing beyond the embayment coastline in regions of localized low across-flow strain rate $\dot{\epsilon}_\perp$. These observations support the notion that, upon exiting embayments, VM facilitates advance in unbuttressed regions and EC trends towards the embayment cutoff, removing unbuttressed ice if present. This is consistent with the idea that EC calves ice at a faster rate when across-flow strain rate $\dot{\epsilon}_\perp$ increases, i.e. upon exiting an embayment and removing the influence of embayment margin stresses. This pattern does not hold

310 for all ice shelves under consideration (namely, Larsen C, where we observe an opposite trend, possibly due to the influence of topographic pinning points such as Gipps Ice Rise), but it represents a simple mechanistic explanation that is consistent with calving law theory.

Based on these results, we recommend that EC and VM be used on a case-by-case basis for modeling Antarctic ice shelves on centennial timescales. However, as climate continues to warm and ice shelves likely retreat deeper within their embayments,
315 across-flow strain rate $\dot{\epsilon}_\perp$ may decrease in regions where the ice flow is channelized through deep troughs with parallel side walls, rendering EC intractable as a long-term solution given that it will consistently readvance the ice front to the embayment coastline under these conditions. Thus, as Antarctic ice shelves become more akin to fjord-confined Greenland glaciers in that they contain a higher proportion of buttressed ice, VM may become a more appropriate choice, as in Choi et al. (2018) for Greenland. This recommendation is not inconsistent with the results of Fig. 6, as Fig. 6 compares against the modern-day
320 scenario where ice fronts generally exist at or downstream of the embayment margin instead of within the embayment. To this end, we also recommend that future numerical experiments investigate how calving will occur as ice shelves retreat upstream of coastlines, where ice is more likely to be highly buttressed. To date, the collapse of Larsen B Ice Shelf is the only such observation of this process occurring, so modeling efforts represent our best opportunity to learn more about this process.

Although simple to conceptualize, our misfit metric involves some important caveats. Most notable is its dependence on
325 observed calving front length. Meandering calving fronts, which have greater lengths than straight calving fronts spanning the same embayment width, will result in a smaller misfit metric since the calving front length is in the denominator. This is true so long as the the misfit area in the numerator does not increase commensurately. For this reason, it is not particularly valuable to compare absolute misfit metric values between different ice shelves which have dissimilar observed calving front lengths.
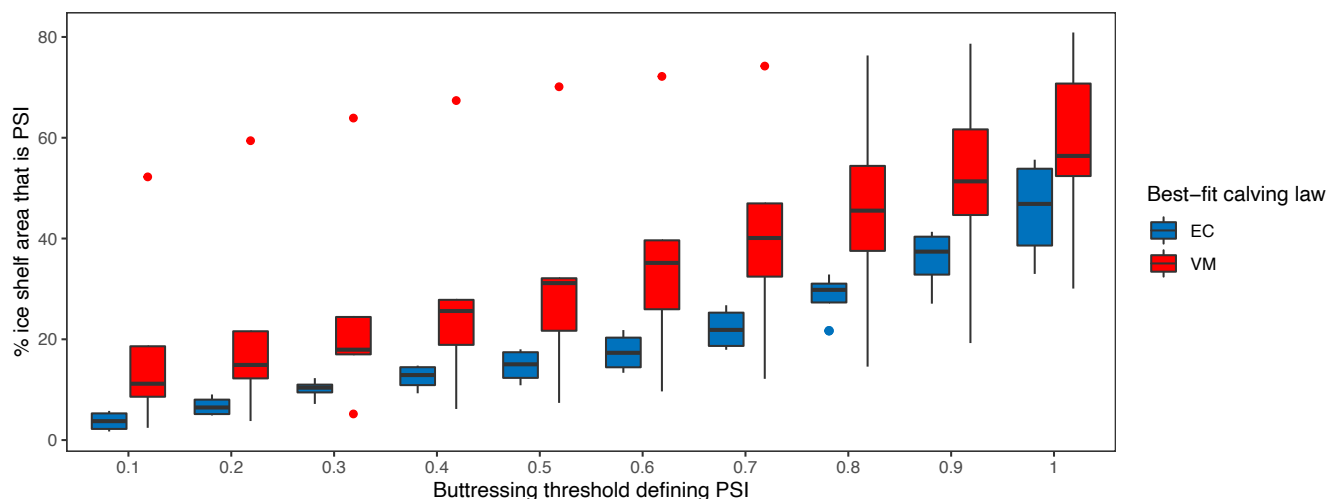
Figure 6. Box-and-whisker plot grouped by eventual best-fit calving law (EC or VM) for different buttressing thresholds defining PSI plotted against the percentage of shelf area that is PSI. Here, PSI fraction is computed just after model initialization (t=0 yrs). Dots represent outliers, with the upper VM outlier being Shackleton Ice Shelf.
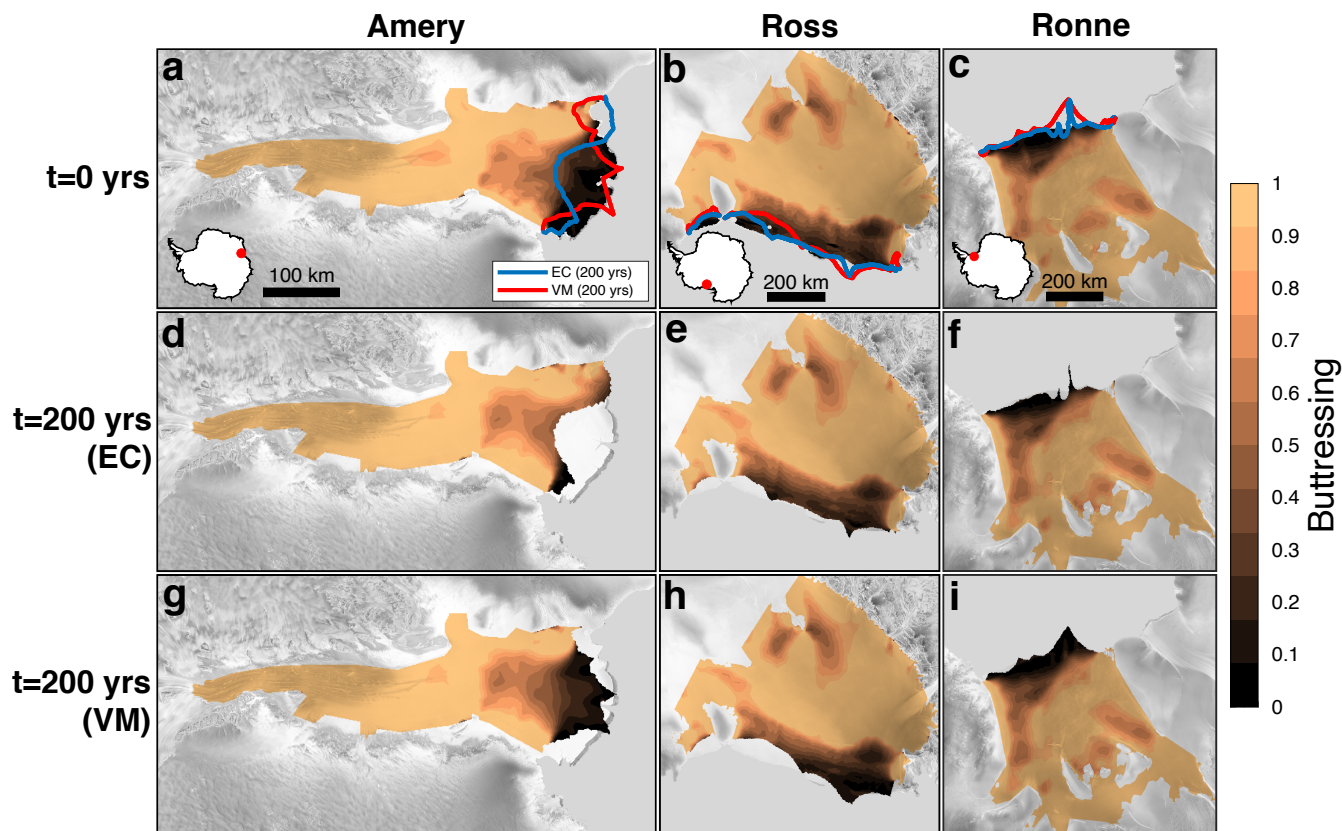
Figure 7. Three ice shelves (Amery, Ross, and Ronne) where the best-fit EC model run removes most unbuttressed ice outside of the embayment **(d-f)** and where the best-fit VM model run maintains an unbuttressed ice extent outside of the embayment **(g-i)**. Here, only floating ice is plotted in colors. Ice shelf location is shown by a red dot on an Antarctica inset. Model results are overlaid with a radar image from RAMP AMM-1 (Jezek, 1999) in grey.

Instead, it is more informative to compare the relative order by which calving laws minimize the misfit metric, as misfit is
330 consistent between each calving law for a given ice shelf. In this sense, calving law order is comparable between ice shelves.
Another limitation of our misfit metric is its inability to distinguish between regions of advance and regions of retreat for a given model run. Retreat and advance contribute equally to the misfit calculation since the area between the the two fronts is unsigned. While most models either mostly retreat or mostly advance (or remain in steady state) for a given tuning parameter value, there are some exceptions (e.g., the best-fit CD run for Larsen C) that preclude easy interpretation. As an alternative to
335 our misfit metric, we computed the Fréchet distance (e.g., Alt and Godau, 1995), a widely used measure of curve similarity, between the modeled and observed fronts. The Fréchet distance may be defined as the greatest distance between ordered pairs of points on two lines. In general, we find that the Fréchet distance closely replicates the results of our misfit metric, such that the calving law which minimizes the misfit is broadly the same for our metric and the Fréchet distance.

5 Conclusions

We evaluate and compare four calving laws for ten ice shelves in Antarctica, relying on an assumption that Antarctic ice shelves tend to maintain a steady state calving front position over decadal timescales. We find that the majority (9 of 10) of modern observed ice shelf fronts are best fit by either the eigencalving (EC) law or the von Mises (VM) law for 200-year 2-D SSA model runs in ISSM. The minimum thickness (MT) law and the crevasse depth (CD) law are largely unsuccessful by our misfit metric. Nominally, the proportion of passive shelf ice (PSI) is a predictor of EC versus VM success for a given ice shelf. This reflects the fact that ice spreads laterally upon exiting an embayment and thus increases in lateral strain rate, prompting the EC law to increase calving rate and limit the ice front to the embayment coastline. No such mechanism occurs for VM, so we suggest that VM is often a better choice for ice shelves that do not terminate at their embayment coastlines. Future work should consider more complex calving laws, such as those incorporating damage criteria or rifting physics, and should address the nature of calving as inevitable retreat of shelf ice into the highly buttressed interiors of embayments occurs. Additionally, once the observational record becomes sufficiently long (∼50 years), supplementary studies should replicate this work without our assumption of a steady state calving front position.

Code and data availability. ISSM is open source and is available at https://issm.jpl.nasa.gov (Version 4.22, last access: June 7, 2023). The initial geometry is from BedMachine v3 (Morlighem et al., 2020) and is available at https://nsidc.org/data/nsidc-0756/versions/3. The code of the simulation and data analyses is available at https://doi.org/10.5281/zenodo.8015164.

Author contributions. JW and MM designed the setup of the numerical experiments. JW conducted the numerical experiments and data analysis, with assistance from MM and GC. JW wrote the first version of the manuscript, with input from MM and GC.

Competing interests. The authors declare that they have no conflict of interest.

Acknowledgements. JW and MM acknowledge support from the National Science Foundation (award no. 2147601), "Collaborative Research: Frameworks: Convergence of Bayesian inverse methods and scientific machine learning in Earth system models through universal differentiable programming." GC is supported by two Heising-Simons Foundation grants (no. 2019-1161 and no. 2021-3059).

References

Alt, H. and Godau, M.: Computing the Fréchet distance between two polygonal curves, Int. J. Comput. Geom. Ap., 5, 75–91, 1995.

Amaral, T., Bartholomaus, T. C., and Enderlin, E. M.: Evaluation of iceberg calving models against observations from Greenland outlet glaciers, J. Geophys. Res.-Earth, 125, 1–29, https://doi.org/10.1029/2019JF005444, 2020.

365   Amundson, J. M. and Truffer, M.: A unifying framework for iceberg-calving models, J. Glaciol., 56, 822–830, https://doi.org/10.3189/002214310794457173, 2010.

Amundson, J. M., Fahnestock, M., Truffer, M., Brown, J., Lüthi, M. P., and Motyka, R. J.: Ice mélange dynamics and implications for terminus stability, Jakobshavn Isbræ, Greenland, J. Geophys. Res.-Earth, 115, https://doi.org/10.1029/2009JF001405, 2010.

Aschwanden, A., Fahnestock, M. A., Truffer, M., Brinkerhoff, D. J., Hock, R., Khroulev, C., Mottram, R., and Khan, S. A.: Contribution of
370   the Greenland Ice Sheet to sea level over the next millennium, Science Advances, 5, eaav9396, https://doi.org/10.1126/sciadv.aav9396, 2019.

Bassis, J. N.: The statistical physics of iceberg calving and the emergence of universal calving laws, J. Glaciol., 57, 3–16, https://doi.org/10.3189/002214311795306745, 2011.

Bassis, J. N. and Jacobs, S.: Diverse calving patterns linked to glacier geometry, Nat. Geosci., 6, 833–836, https://doi.org/10.1038/ngeo1887,
375   2013.

Benn, D. I., Aström, J., Zwinger, T., Todd, J., Nick, F. M., Cook, S., Hulton, N. R. J., and Luckman, A.: 'Calving laws', 'sliding laws' and the stability of tidewater glaciers, Ann. Glaciol., 46, 123–130, https://doi.org/10.3189/172756407782871161, 2007a.

Benn, D. I., Warren, C. R., and Mottram, R. H.: Calving processes and the dynamics of calving glaciers, Earth-Sci. Rev., 82, 143–179, https://doi.org/10.1016/j.earscirev.2007.02.002, 2007b.

380   Benn, D. I., Åström, J., Zwinger, T., Todd, J., Nick, F. M., Cook, S., Hulton, N. R., and Luckman, A.: Melt-under-cutting and buoyancy-driven calving from tidewater glaciers: new insights from discrete element and continuum model simulations, J. Glaciol., 63, 691–702, https://doi.org/10.1017/jog.2017.41, 2017.

Bondzio, J. H., Seroussi, H., Morlighem, M., Kleiner, T., Rückamp, M., Humbert, A., and Larour, E. Y.: Modelling calving front dynamics using a level-set method: Application to Jakobshavn Isbræ, West Greenland, The Cryosphere, 10, 497–510, https://doi.org/10.5194/TC-
385   10-497-2016, 2016.

Borstad, C., Khazendar, A., Scheuchl, B., Morlighem, M., Larour, E., and Rignot, E.: A constitutive framework for predicting weakening and reduced buttressing of ice shelves based on observations of the progressive deterioration of the remnant Larsen B Ice Shelf, Geophys. Res. Lett., 43, 2027–2035, https://doi.org/10.1002/2015GL067365, 2016.

Brown, C. S., Meier, M. F., and Post, A.: Calving speed of Alaska tidewater glaciers, with application to Columbia Glacier, U.S. Geological
390   Survey Professional Paper, 1258 C, 13 pp., https://doi.org/10.3133/pp1258c, 1983.

Cassotto, R., Fahnestock, M., Amundson, J. M., Truffer, M., and Joughin, I.: Seasonal and interannual variations in ice melange and its impact on terminus stability, Jakobshavn Isbræ, Greenland, J. Glaciol., 61, 76–88, https://doi.org/10.3189/2015JoG13J235, 2015.

Choi, Y., Morlighem, M., Wood, M., and Bondzio, J. H.: Comparison of four calving laws to model Greenland outlet glaciers, The Cryosphere, 12, 3735–3746, https://doi.org/10.5194/tc-12-3735-2018, 2018.

395   Duddu, R., Bassis, J. N., and Waisman, H.: A numerical investigation of surface crevasse propagation in glaciers using nonlocal continuum damage mechanics, Geophys. Res. Lett., 40, 3064–3068, https://doi.org/10.1002/GRL.50602, 2013.

Fricker, H. A., Young, N. W., Allison, I., and Coleman, R.: Iceberg calving from the Amery Ice Shelf, East Antarctica, Ann. Glaciol., 34, 241–246, https://doi.org/10.3189/172756402781817581, 2002.

Fürst, J. J., Durand, G., Gillet-Chaulet, F., Tavard, L., Rankl, M., Braun, M., and Gagliardini, O.: The safety band of Antarctic ice shelves,
400   Nat. Clim. Change, 6, 479–482, https://doi.org/10.1038/nclimate2912, 2016.

Gagliardini, O., Durand, G., Zwinger, T., Hindmarsh, R. C. A., and Le Meur, E.: Coupling of ice-shelf melting and buttressing is a key process in ice-sheets dynamics, Geophys. Res. Lett., 37, 1–5, https://doi.org/10.1029/2010GL043334, 2010.

Hughes, T.: Theoretical calving rates from glaciers along ice walls grounded in water of variable depths, J. Glaciol., 38, 282–294, https://doi.org/10.3189/S0022143000003695, 1992.

405 Jezek, K. C.: Glaciological properties of the Antarctic ice sheet from RADARSAT-1 synthetic aperture radar imagery, Ann. Glaciol., 29, 286–290, https://doi.org/10.3189/172756499781820969, 1999.

Krug, J., Weiss, J., Gagliardini, O., and Durand, G.: Combining damage and fracture mechanics to model calving, The Cryosphere, 8, 2101–2117, https://doi.org/10.5194/TC-8-2101-2014, 2014.

Larour, E., Seroussi, H., Morlighem, M., and Rignot, E.: Continental scale, high order, high spatial resolution, ice sheet modeling using the
410   Ice Sheet System Model (ISSM), J. Geophys. Res.-Earth, 117, https://doi.org/10.1029/2011JF002140, 2012.

Levermann, A., Albrecht, T., Winkelmann, R., Martin, M. A., Haseloff, M., and Joughin, I.: Kinematic first-order Calving Law implies potential for abrupt ice-shelf retreat, The Cryosphere, 6, 273–286, https://doi.org/10.5194/tc-6-273-2012, 2012.

MacAyeal, D. R.: Large-scale ice flow over a viscous basal sediment: Theory and application to ice stream B, Antarctica, J. Geophys. Res.-Sol. Ea., 94, 4071–4087, 1989.

415 Meier, M. F. and Post, A.: Fast Tidewater Glaciers, J Geophys. Res., 92, 9051–9058, https://doi.org/10.1029/JB092iB09p09051, 1987.

Mercenier, R., Lüthi, M. P., and Vieli, A.: Calving relation for tidewater glaciers based on detailed stress field analysis, The Cryosphere, 12, 721–739, https://doi.org/10.5194/TC-12-721-2018, 2018.

Morland, L. and Zainuddin, R.: Plane and radial ice-shelf flow with prescribed temperature profile, in: Dynamics of the West Antarctic Ice Sheet: Proceedings of a Workshop held in Utrecht, May 6–8, 1985, pp. 117–140, 1987.

420 Morlighem, M., Bondzio, J., Seroussi, H., Rignot, E., Larour, E., Humbert, A., and Rebuffi, S.: Modeling of Store Gletscher's calving dynamics, West Greenland, in response to ocean thermal forcing, The Cryosphere, 43, 2659–2666, https://doi.org/10.1002/2016GL067695, 2016.

Morlighem, M., Rignot, E., Binder, T., Blankenship, D., Drews, R., Eagles, G., Eisen, O., Ferraccioli, F., Forsberg, R., Fretwell, P., et al.: Deep glacial troughs and stabilizing ridges unveiled beneath the margins of the Antarctic ice sheet, Nat. Geosci., 13, 132–137,
425   https://doi.org/10.1038/s41561-019-0510-8, 2020.

Mouginot, J., Rignot, E., and Scheuchl, B.: Continent-wide, interferometric SAR phase, mapping of Antarctic ice velocity, Geophys. Res. Lett., 46, 9710–9718, https://doi.org/10.1029/2019GL083826, 2019.

Nick, F. M., Van Der Veen, C. J., Vieli, A., and Benn, D. I.: A physically based calving model applied to marine outlet glaciers and implications for the glacier dynamics, J. Glaciol., 56, 781–794, https://doi.org/10.3189/002214310794457344, 2010.

430 Noël, B., Van De Berg, W., Van Meijgaard, E., Kuipers Munneke, P., Van De Wal, R., and Van Den Broeke, M.: Evaluation of the updated regional climate model RACMO2. 3: summer snowfall impact on the Greenland Ice Sheet, The Cryosphere, 9, 1831–1844, https://doi.org/10.5194/tc-9-1831-2015, 2015.

Pfeffer, W. T., Dyurgerov, M., Kaplan, M., Dwyer, J., Sassolas, C., Jennings, A., Raup, B., and Manley, W.: Numerical modeling of Late Glacial Laurentide advance of ice across Hudson Strait: Insights into terrestrial and marine geology, mass balance, and calving flux, Paleoceanography, 12, 97–110, https://doi.org/10.1029/96PA03065, 1997.

Pollard, D., DeConto, R. M., and Alley, R. B.: Potential Antarctic Ice Sheet retreat driven by hydrofracturing and ice cliff failure, Earth Planet Sc. Lett., 412, 112–121, https://doi.org/10.1016/j.epsl.2014.12.035, 2015.

Rignot, E., Rivera, A., and Casassa, G.: Contribution of the Patagonia Icefields of South America to sea level rise, Science, 302, 434–437, https://doi.org/10.1126/science.1087393, 2003.

Rignot, E., Jacobs, S., Mouginot, J., and Scheuchl, B.: Ice-shelf melting around Antarctica, Science, 341, 266–270, https://doi.org/10.1126/science.1235798, 2013.

Tournadre, J., Girard-Ardhuin, F., and Legrésy, B.: Antarctic icebergs distributions, 2002–2010, J. Geophys. Res.-Oceans, 117, https://doi.org/10.1029/2011JC007441, 2012.

Van Der Veen, C.: Tidewater calving, J. Glaciol., 42, 375–385, https://doi.org/10.3189/s0022143000004226, 1996.

Vieli, A., Funk, M., and Blatter, H.: Flow dynamics of tidewater glaciers: a numerical modelling approach, J. Glaciol., 47, 595–606, https://doi.org/10.3189/172756501781831747, 2001.

Wang, S., Liu, H., Jezek, K., Alley, R. B., Wang, L., Alexander, P., and Huang, Y.: Controls on Larsen C Ice Shelf retreat from a 60-year satellite data record, J. Geophys. Res.-Earth, 127, e2021JF006 346, https://doi.org/10.1029/2021JF006346, 2022.

Yu, H., Rignot, E., Morlighem, M., and Seroussi, H.: Iceberg calving of Thwaites Glacier, West Antarctica: Full-stokes modeling combined with linear elastic fracture mechanics, The Cryosphere, 11, 1283–1296, https://doi.org/10.5194/TC-11-1283-2017, 2017.

Zhang, T., Price, S. F., Hoffman, M. J., Perego, M., and Asay-Davis, X.: Diagnosing the sensitivity of grounding-line flux to changes in sub-ice-shelf melting, The Cryosphere, 14, 3407–3424, https://doi.org/10.5194/tc-14-3407-2020, 2020.